

<https://doi.org/10.1038/s41612-025-01118-5>

The significant contribution of biomass burning to methanol-soluble nitrogenous organics and its evolution during the highly-humid haze event in urban Wuhan



A list of authors and their affiliations appears at the end of the paper

Fine particle (PM_{2.5}) controls in China have achieved great success these years, but heavy haze pollution still occurs occasionally. The sources and evolution of the complex organic mixtures remain poorly resolved. We collected 46 PM_{2.5} samples during a 12-day severe haze episode in Wuhan, a megacity in central China. We analyzed the molecular-level organic composition and functional groups with high-performance liquid chromatography-orbitrap tandem mass spectrometry (HPLC-Orbitrap MS/MS). The methanol-soluble nitrogenous organics (ONs) contributed 87.6% and 52.5% of total signal intensity in positive electrospray ionization (ESI+) mode and negative electrospray ionization (ESI-) mode, respectively. Through source apportionment and backward trajectory analysis, we found great contribution of biomass burning (~21.2% of ONs in ESI+ mode and 78.2% in ESI- mode) and significant aqueous/heterogeneous products (~71.2% of ONs in ESI+ mode and 18.7% in ESI- mode) during the prolonged, highly-humid evolution (relative humidity ~86.8% lasting for 7 days). We identified C6–C12 amines and C6–C9 nitrophenols as possible molecular markers for biomass burning emissions, while C17–C19 amine oligomers and dicarboxylic acids as secondary markers from heterogeneous/aqueous reactions. The evolution may include three pathways: (1) polymerization of amines with an oxygenated molecule to form long-chain oxygenated amine oligomers; (2) ring-opening fragmentation of nitrophenols to form dicarboxylic acids; (3) ring-retaining functionalization of nitroaromatics to form nitroaromatic carboxylic acids. Pathway 3 has rarely been observed in ambient air, which is possibly related with the extremely high humidity during the periods and deserves further studies. Lastly, we found that ~39.3% of ON compounds had isomers, and ~43.7% of these isomers had distinct timeseries and originated from different sources, strengthening the necessity of measuring isomers. With the help of tandem high-resolution mass spectrometry, this study provides valuable datasets for the molecular and structural information on sources and evolutions of ONs under the highly-humid urban atmospheres.

Particulate nitrogenous organics (ONs) comprise a large fraction of urban atmospheric organic aerosols¹. They exert a great role in particle hygroscopicity², particle light-absorption³, and atmospheric nitrogen cycle⁴. Atmosphere particulate ONs originate from a wide range of primary sources^{5–8} (i.e., biomass burnings, vehicle emissions, industrial emissions, coal combustion, and soil dust emission) and secondary formations^{9,10} (i.e., photooxidation and heterogeneous reactions), resulting in complex

mixtures. Previous studies have reported that ONs with low oxygen content mostly contain amine groups¹¹, while those with high oxygen content may contain nitro (-NO₂) or nitrooxy (-ONO₂) group^{12,13}. Some ONs containing sulfur, generally recognized as nitrooxy-organosulfates¹⁴, are proposed to be formed via the heterogeneous oxidation under high NO_x and SO₂ levels^{15–17}. However, the characteristics and evolution of ONs vary across cities and seasons^{18–21}, indicating the significant differences in sources and

✉ e-mail: lixiaoxiao@whu.edu.cn; chenghr@whu.edu.cn

atmospheric oxidations. Digging into the molecular-level chemical components of ONs can provide useful information on their primary sources, secondary formations, and atmospheric impacts.

The explorations of molecular-level information on ONs have been facilitated with the employment of ultrahigh-resolution mass spectrometers (UHRMS), such as Orbitrap and Fourier-transform ion cyclotron resonance mass spectrometry^{22,23}. As hundreds of ONs were usually identified in the ambient atmosphere, various parameters have been proposed as representatives to study the bulk characteristics of ONs, such as double bond equivalence (DBE) and oxygen to carbon element number ratios (O/C)^{19–21}. However, such parameters can only represent the bulk characteristic of ONs, they cannot distinguish isomers and functional groups, and thus provide very limited information for mechanistic studies. Alternatively, tandem mass analysis can provide the information of functional group information. Some studies used high performance liquid chromatography coupled with tandem mass spectrometry (HPLC-MS/MS) to differentiate isomers and determine their structures^{24,25}. HPLC allows the isomers to be separated and enter the MS at different times. Then MS/MS uses a certain amount of energy to break up the molecules, and the fragments are used to distinguish the structural composition^{26–29}. Previously, it has been used to characterize the functional groups of atmospheric organic aerosol^{21,30}.

Functional groups can provide useful information on the origins and evolution of compounds. For example, nitroaromatic groups can be emitted directly through diesel exhaust, wood combustion, and consumer product solvent emissions^{25,31}. They can also be formed chemically, e.g., by nighttime aqueous-phase nitration of catechols with HNO₂³² or gas-phase oxidation of phenolic compounds by OH•/NO₃• followed by further nitration with NO₂³³. These compounds can undergo further reactions in the atmosphere. Photolysis and radical oxidation are the main modes of nitrophenol degradation, which may form carboxylic acids and other oxygen-containing compounds^{34–37}. Organonitrate groups are typical secondary products, they are formed by the oxidation of volatile organic compounds (VOCs) by NO₃• during nighttime or by reaction with OH•/O₃ and subsequent NO during daytime^{38,39}. Almost all secondary ONs have oxygen-containing functional groups such as alcohol, carbonyl, carboxylic acid, ether, and ester⁴⁰. Different nitrogen-containing groups may indicate different routes of secondary aerosol formation^{30,41,42}.

The megacity of Wuhan is characterized by intense primary emissions, highly-humid air conditions, and frequent transport influences. Although the air quality in Wuhan has improved a lot during last 20 years^{43,44}, severe haze pollution still happens occasionally^{45,46}, and the mechanisms are not entirely clear. Firstly, as the most populous city, an important industrial base, and a comprehensive transportation hub in central China^{47,48}, Wuhan holds many heavy industries including steel, glass, cement, and chemical industry, and has a large number of motor vehicles, boats, and ships, leading to a vast amount of primary pollutant emissions⁴⁹. Intensive agricultural activities in the Jiangnan Plain (especially rice and rapeseed cultivation) result in a large amount of straw residue, and open burning is the main treatment method^{50,51}. Hubei Province has achieved some success in strictly controlling straw burning through satellite monitoring and administrative penalties, but due to the lack of alternative means of utilization (e.g., high cost of straw recycling, immature market for organic fertilizers), burning is still the main method of disposal^{52,53}. Thus, Wuhan is also influenced significantly by the biomass burning. Secondly, Wuhan is characterized by a humid subtropical monsoon climate and densely dotted with rivers and lakes, leading to highly humid air conditions with yearly-average RH > 70% and facilitating the secondary heterogeneous or aqueous reactions. Thirdly, Wuhan and its surrounding cities and provinces are surrounded by mountains to the east, west, and south, resulting in weak horizontal atmospheric flow and slow dispersion of pollutants⁵⁴. Due to its terrain, Wuhan serves as a conduit for the intrusion of cold northern air and moist eastern air, facilitating the transport of pollutants to this area. Previous studies on PM_{2.5} in Wuhan have been extensive, but the molecular-level particulate organic compositions in Wuhan have not been reported, especially during the haze evolution.

In this study, for a 12-day long-lasting high-humid haze pollution process in Wuhan, we sampled PM_{2.5} and analyzed molecular-level organic aerosols using HPLC-Orbitrap MS/MS. Four samples were collected each day. This provided a more-detailed time series of compound variations during the haze episode. We found that ONs constituted a large proportion of organic aerosol in Wuhan. The functional groups of ONs were analyzed. Combining the backward trajectory analysis and chemical tracers, we revealed that biomass burning and its evolution contributed greatly to the haze pollution in Wuhan.

Results and discussion

Molecular-level organic composition and functional groups in particles

Using HPLC-Orbitrap MS/MS, we identified approximately 2200 and 2100 compounds (isomers counted as distinct compounds) in ESI+ and ESI- modes, respectively, with total signal intensities of 2.85E9 and 3.04E8. These compounds were selected due to their high signal intensity, high signal to noise ratio, as well as good peak shape. It is noteworthy that, as methanol was chosen as the extraction solvent in this study, only methanol-soluble organic compounds were investigated. Comparative experiments using three commonly-used solvents, methanol, acetonitrile, and acetonitrile/water (8:2, v/v), revealed that methanol extracted the largest amount of organic species (as detailed in Methods section, Table S1). The component distributions extracted by methanol and acetonitrile were similar, while those extracted by acetonitrile/water (8:2, v/v) were quite different (Fig. S1). For instance, methanol and acetonitrile showed higher selectivity toward CHON species in ESI+ mode and lower sensitivity to CHOS/CHONS species in ESI- mode compared to acetonitrile/water. Detailed comparison can be found in Method Section and the SI.

The compounds were categorized according to their elemental composition, as illustrated in different colors in the mass defect plots (Fig. 1a, d). Clear homologous sequences can be observed for different categories. In ESI+ mode, the species with the highest peak area were CHON (72.8%), followed by CHO (11.0%), CHN (10.2%), CHONS (4.6%), and others (1.4%), including CHOS, CH, CHS, CHNS) (Fig. 1b). In ESI- mode, CHON also represented the highest peak area (50.3%), followed by CHO (27.1%), CHOS (22.6%), and CHONS (2.2%) (Fig. 1e). In summary, nitrogenous organics (ONs) exhibited dominant proportions in both ESI+ (~87.6%) and ESI- mode (~52.5%).

In the ESI+ mode, ONs were predominantly characterized by homologous sequences with a lower oxygen content (≤ 2 oxygen atoms) and lower degree of unsaturation (averagely ~ 3.9), mostly containing amine/amide groups. For CHON, C_nH_{2n+1}ON was the most abundant (accounting for 19.1% in total signal intensity), followed by C_nH_{2n-1}ON (15.9%), C_nH_{2n+3}O₂N (11.5%), and C_nH_{2n+3}ON (3.3%). For CHN, C_nH_{2n-13}N was the most abundant (18.4%), followed by C_nH_{2n+3}N (14.8%), and C_nH_{2n-2}N₂ (14.1%). For CHONS, the most abundant homologous sequence was C_nH_{2n}O₂N₂S₂ (1.3%). In terms of functional groups, ONs in ESI+ mode mainly contained amine (75.5%), amide (16.0%), azole (2.8%), pyridine (2.4%), N-N (1.5%), nitrile (1.4%), isocyanate (0.3%), and N=N (0.2%). Most ONs in ESI+ mode (65.2%) contain no ring, 20.8% of ONs contain aromatic ring, and 14.1% contain non-aromatic ring.

In the ESI- mode, ONs were predominantly represented by homologous sequences with higher oxygen content (≥ 3 oxygen atoms) and higher degree of unsaturation (averagely ~ 4.7), mostly containing nitroaromatic group. For CHON, C_nH_{2n-7}O₃N (18.7%) was the most abundant, followed by C_nH_{2n-7}O₄N (8.7%), C_nH_{2n}O₃N₃ (3.0%), C_nH_{2n-1}O₃N (2.4%), C_nH_{2n-8}O₅N₂ (2.2%), and C_nH_{2n-9}O₅N (2.1%). For CHONS, the most abundant homologous sequence was C_nH_{2n-3}O₇NS (2.0%). In terms of functional groups, ONs in ESI- mode mainly contained nitroaromatic (72.0%), followed by amine (15.6%), amide (9.1%), azole (1.4%), pyridine (1.3%), and isocyanate (0.7%). Most ONs in ESI- mode (75.9%) contain aromatic ring, 13.3% of ONs contain non-aromatic ring, and 10.8% contain no ring.

To sum up, although ESI+ and ESI- mode could detect similar categories, their functional groups are entirely different, resulting in different

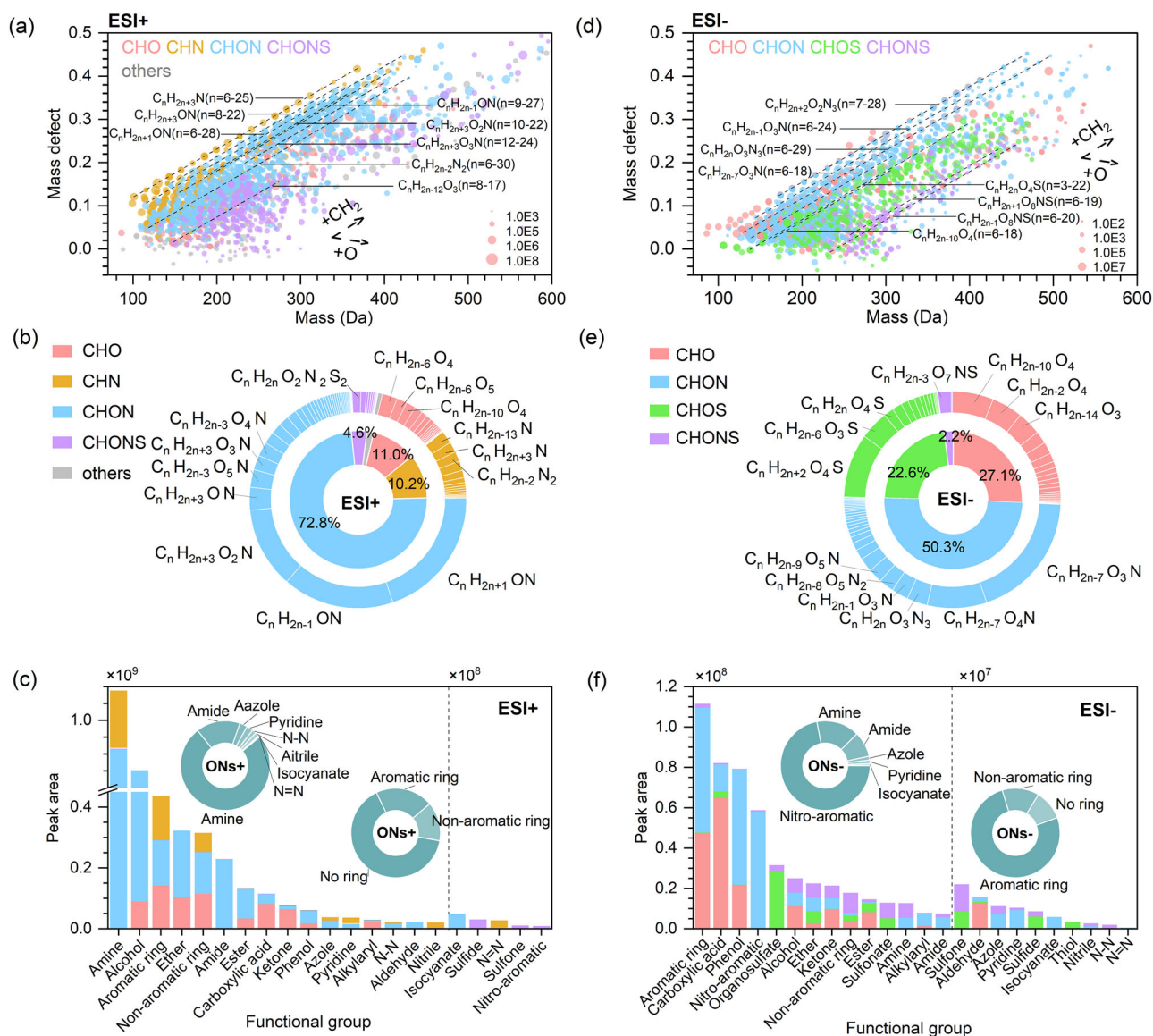


Fig. 1 | Species and functional group composition of PM_{2.5} in Wuhan, measured by HPLC-Orbitrap MS/MS. a, d Mass defect plot of the detected compounds. The diameter of the point is proportional to the peak area. **b, e** Peak area fractions of different species and homologous sequences, represented by the inner and outer

circle, respectively. **c, f** Functional group peak area for different categories. ONs + / ONs- represents the nitrogenous organic detected in the positive/negative electrospray ionization mode and the peak area mentioned above refers to the average peak area of all collected PM_{2.5} samples.

oxygen contents and degree of unsaturation. ONs in ESI+ mode were dominated by aliphatic amines and amides, while those in ESI- mode were dominated by nitroaromatics. Besides ONs, CHO compounds represented the second-largest proportion in both modes. They were mainly ethers and alcohols in ESI+ mode, while mainly carboxylic acids (of which multi-carboxylic acids account for 54.0%) in ESI- mode. Sulfur-containing organics in ESI- mode were dominated by organosulfates, while those in ESI+ mode were mainly sulfides.

Compared with other urban cities in China, ON fraction, especially CHON fraction, in Wuhan was at a relatively high level. For instance, the CHON fraction in Wangdu⁵⁵, Shanghai^{19,56}, Changchun, Guangzhou⁵⁶, and Beijing³¹, varied between 9.0–46.5% in ESI+ mode and 6.0–55.0% in ESI- mode. In contrast, CHON fraction in Wuhan reached 72.8% in ESI+ mode and 50.3% in ESI- mode, respectively. Seasonal variations in previous studies showed that CHON fraction typically increased during wintertime^{19,20}, but even considering this, the CHON fraction in Wuhan was still relatively higher. A possible reason was the high NO₂ concentration in Wuhan, which was averaged 71 μg/m³ during the sampling period. We compared the ON

fraction (including CHON, CHONS, and CHN) with NO₂ concentration in different studies which used methanol or acetonitrile as solvent (Fig. 2). We found that the ON fraction generally showed an increasing trend as the NO₂ concentration increased. And it is notably that even considering the higher NO₂ concentration, the fraction of CHON in ESI+ mode in Wuhan was still significantly higher. The high ON fraction in Wuhan may also be attributed to the sources and will be explored in the following analysis.

The functional group composition in Wuhan shared some similarities with other cities, while exhibiting its distinct characteristics. The main functional groups in previous studies included alcohol (15–49%), carboxylic acid (19–59%), ether (10–23%), etc.^{30,40,57}. The fraction of alcohol (28%), carboxylic acid (21%), and ether (11%) in Wuhan were within the reported ranges. But there were some differences. We measured higher levels of amine (32%) than the previously reported 11–28%^{30,40,58,59}. In addition, organonitrates were observed at Atlanta (1–11%)⁴⁰, 5–12% over the southeastern United State⁵⁷, and 3–8% in a previous study in Wuhan³⁰. However, we hardly detected organonitrates (the appearance time was less than 10, and thus not further analyzed) in this study, which may result from

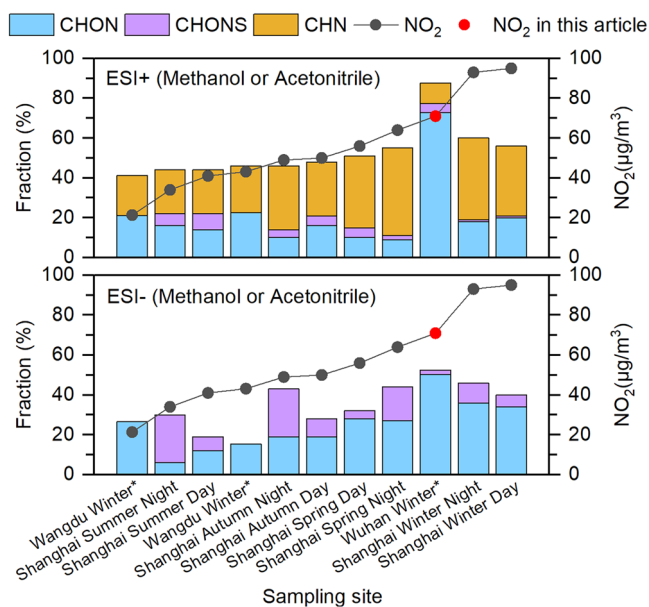


Fig. 2 | ON fraction with NO₂ concentration in different cities. The cities include Shanghai^{19,56}, Wangdu⁵⁵ and Wuhan (this article). “*” indicates methanol as the extraction solvent while others used acetonitrile.

the hydrolysis of organonitrate during the high humidity in this sampling period or the degradation on the filters during sampling^{60,61}.

Source apportionment of particulate organics

To explore the sources of organic pollutants, we applied K-Means clustering to classify the identified organics into 3 classes in ESI+ and ESI- modes respectively, based on their similarities in timeseries (Fig. 3a, b). Additionally, to explore the meteorological effects for the haze formation, we divided the haze event into 4 periods based on analysis of backward trajectories, fluctuations in temperature and humidity, and changes in wind speed and direction (Fig. 3c, d). We also compared the classified sources with SOR (ratio of particulate sulfate to the sum of particulate sulfate and gaseous SO₂, calculated as Eq. S1) and NOR (ratio of particulate nitrate to the sum of particulate nitrate and gaseous NO₂, calculated as Eq. S2) to explore the role of secondary formations (Fig. 3e). From the combined analysis, we preliminarily classified Class 1, Class 2, and Class 3 as primary organic aerosol-like (POA-like) class, biomass burning organic aerosol-like (BBOA-like) class, and secondary organic aerosol-like (SOA-like) class, respectively.

Class 1 mainly originated from high local emissions with influences from long-range transported dust. As shown in Fig. 3a, b, the time series of Class 1+ and Class 1- both exhibited relatively high concentrations at the beginning, followed by decreases of ~56.1% and ~68.4%, respectively, until the end of the study period. Class 1+ and Class 1- showed significant positive correlations with NO₂ and SO₂ ($r = 0.49-0.78$, $p < 0.05$, Figs. S2-S3), which were typical primary gases from combustion emissions⁶²⁻⁶⁴. SOR and NOR remained below 0.2 during Periods 1-2, suggesting particle dominance by primary emissions (Fig. 3e). Class 1+ and Class 1- both peaked during Period 1, accompanied by air masses showing long-range transport from the high-altitude northwest. The strong correlation between Class 1+ and Ca²⁺ ($r = 0.67$, $p < 0.05$, Fig. S3) suggested that the northwestern air masses may contain dust.

Class 2 mainly originated from primary biomass burning in south-eastern Hubei and northern Jiangxi. Class 2+ and Class 2- both exhibited a sharp peak between Jan. 15th and Jan. 16th, and remained low at other periods. This trend showed a significant positive correlation with Na⁺ ($r = 0.33-0.54$, $p < 0.05$, Fig. S3), which could be released from wood and straw combustion⁶⁵ and originated from similar sources with commonly-used biomass burning tracer K⁺ in inland cities^{66,67}. Class 2+ and Class 2- both reached the highest during Period 2, with dominant air trajectories of short-range transport from

the south and southeast. The air masses started at lower altitudes, passing through the northern Jiangxi and the southeastern part of Hubei, where high densities of fire hotspots were observed.

Class 3 mainly represented the secondary transformations occurring in highly-humid environment. In contrast to the high-to-low trend observed in the first two classes, Class 3+ and Class 3- exhibited relatively low concentrations initially, followed by a gradual increase and a significant rise on Jan. 18th. They showed strong positive correlations with inorganic salts including SO₄²⁻ ($r = 0.34-0.57$, $p < 0.05$, Figs. S2-S3) and NO₃⁻ ($r = 0.41$, $p < 0.05$ with Class 3-, Figs. S2-S3) and, which were mainly formed via secondary transformation from NO₂, and SO₂ respectively^{68,69}. Class 3 peaked during the highly humid Period 3, where the air masses were mainly from low-altitude local origins. RH reached ~86.8%, much higher than Period 1 (~46.8%) and Period 2 (~66.8%). Simultaneously, PM_{2.5}, SOR, and NOR continued to increase, while primary pollutants (e.g., NO₂ and SO₂) decreased. During Period 4, under the influence of cold air, Wuhan experienced heavy snowfall process, and the PM_{2.5} pollution was cleared.

Composition of particulate organics from different sources

The ON composition significantly differed among the three classes. In ESI+ mode (Fig. 4a), CHON compounds were the most abundant in the SOA-like Class 3+ (83.7%), especially for CHON_{>275Da}, which accounted for 70.3% in Class 3+, far exceeding the fractions of 1.8% and 18.4% in the other two classes. The CHON_{>275Da} appearing in Class 3+ were mainly amines with oxygen-containing groups, including alcohol, ether, carboxylic acid and ketone (Fig. 4c). For comparison, CHN compounds were the most abundant in BBOA-like Class 2+. Especially for CHN_{<180Da} (mainly amines), which accounted for 25.5% in Class 2+, but their signals nearly disappeared in the secondary-like Class 3+, with only 0.7% contribution. CHN_{<180Da} were mainly amines with no oxygen-containing groups. CHONS compounds were the most abundant in Class 1+ (9.9%), while lower in Class 2+ (2.2%) and Class 3+ (0.2%), indicating their origin from primary sources.

In ESI- mode (Fig. 4b), CHON compounds were the most abundant in the BBOA-like Class 2- (71.8%), far exceeding the fractions of 21.7% and 9.7% in the other two classes. The CHON compounds in Class 2- mainly consisted of aromatic ring, phenol, and nitro-aromatic compounds (Fig. 4d), indicating the dominance of nitrophenols. For comparison, CHO compounds accounted for 64.9% of SOA-like Class 3-, significantly higher than the other two classes. Specifically, CHO_{<150Da} were observed almost exclusively in SOA-like Class 3-. In sight of the functional groups, multi-carboxylic acid groups were dominantly distributed in SOA-like Class 3-. These observations may be associated with secondary formation processes, which will be further investigated in the following sections.

Based on the above analysis, we proposed that the high ONs in Wuhan might be related to (1) high biomass burning contribution. As 78.2% of ONs (mostly nitrophenols) in ESI- mode and 21.2% of ONs (mostly amines) in ESI+ mode are associated with biomass burning (Fig. 4c, d). Since backward trajectory analysis indicates both inter-provincial and intra-provincial biomass burning influences, regional joint prevention and control is crucial for mitigating severe haze. (2) high NO_x concentration and high humidity in Wuhan, enhancing N-containing aqueous/heterogeneous reactions. As 71.2% ONs in ESI+ mode and 18.7% ONs in ESI- mode are associated with secondary evolutions under high RH. (Fig. 4c, d). Given the large contribution of secondary ONs, emission controls should not only target primary sources (e.g., biomass burning) but also focus on precursors (e.g., amines, nitroaromatics) that drive SOA formation.

From the above analysis for Fig. 4, we identified a series of high-intensity representative compounds which can potentially act as sources markers (Table 1). (1) CHN_{<180Da} compounds in ESI+ mode (No. 1-17) may serve as tracers for biomass burning. They are mainly composed of C6-C12 amines. Previous studies have reported that biomass burning is an important source of amines in Yangtze River Delta (Shanghai and Nanjing, China), Pearl River Delta (Guangzhou)⁷⁰, northwest Atlantic Ocean⁷¹ and southeastern US⁷². (2) CHON_{>275Da} compounds in ESI+ mode (No. 18-20)

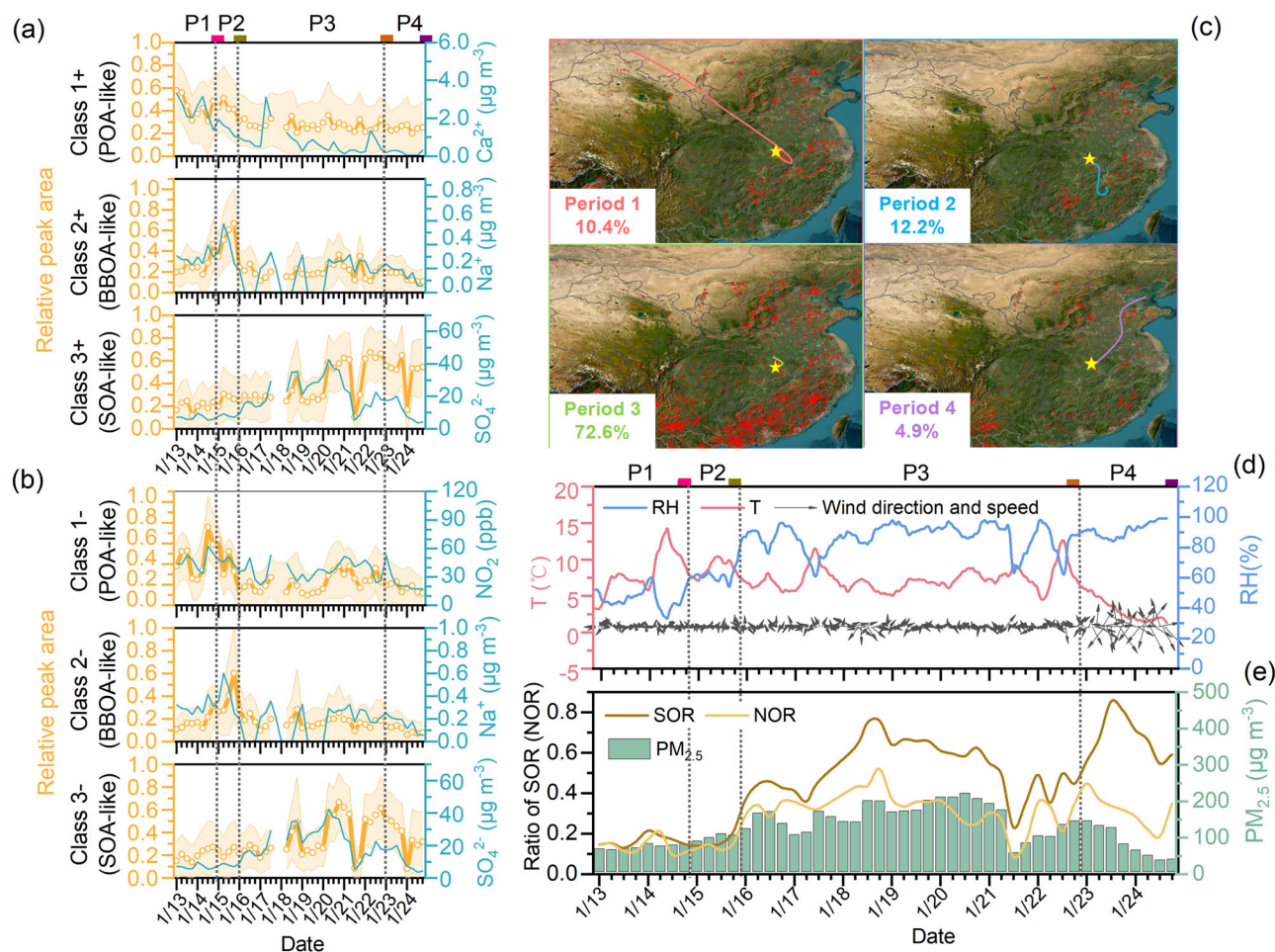


Fig. 3 | K-means clustering with compounds time series, back trajectory with fire points and parameter variation in haze event. a, b Average time series of each class with standard deviation error area and representative compounds related to each class in two modes. POA-like, BBOA-like, and SOA-like refer to primary organic aerosol-like, biomass burning organic aerosol-like, and secondary organic aerosol-

like, respectively. **c** Back trajectory and fire spot map with corresponding clustered air masses. **d** Variation of temperature, RH, wind speed, and wind direction. **e** Variation of Sulfur oxidation ratio (SOR), nitrogen oxidation ratio (NOR), and $PM_{2.5}$ concentration.

may serve as tracers for heterogeneous/aqueous reactions. They are mainly composed of C17–C19 amines containing alcohol or carboxylic acid groups. (3) CHON compounds containing nitroaromatic groups in ESI- mode (No. 21–36) may serve as tracers for biomass burning. They are mainly composed of C6–C9 nitrophenols. Many of them are established tracers of biomass burning in previous studies^{73–78}, such as $C_6H_5NO_4$ and $C_7H_7NO_4$. (4) Dicarboxylic acids in ESI- mode, including CHO compounds (No. 37–43) and CHON compounds (No. 44–46) may serve as tracers for heterogeneous/aqueous reactions. Overall, some of the above tracers have been previously reported while others are not. The list needs to be verified under broader atmospheric environments, with the help of MS/MS analysis to identify the functional groups.

Evolution of the organic components under the highly-humid atmosphere

As previously discussed, abundant ONs from biomass burning were identified in Period 2. During the transition from Period 2 to Period 3, under an average ambient RH of $\sim 87\%$, the biomass burning-related ONs diminished while the secondary ON concentration increased. In Period 3, aerosol liquid water (ALW), as simulated by ISORROPIA II (as detailed in the Methods), averagely reached up to ~ 15.7 times of $PM_{2.5}$ dry volume (Fig. S4), indicating a significant extent of heterogeneous/aqueous-phase reactions^{79,80}. Under such high RH and high ALW, the gas phase oxidation would be suppressed due to the uptake of gas-phase oxidants to the particle phase⁸¹

and reduced radiation under the high wet aerosol mass^{82,83}. The rise of secondary ONs was accompanied by increased SOR and NOR (Fig. 3). Previous studies have indicated that under high RH levels ($\geq 60\%$), particulate nitrate and sulfate are predominantly formed via heterogeneous/aqueous-phase reactions^{84,85}. In summary, we hypothesize that the secondary ONs observed from Period 2 to Period 3 were mainly related to heterogeneous-/aqueous-phase reactions, while the possibility of gas-phase oxidation followed by partitioning was not excluded. Three potential evolution pathways are proposed, as illustrated in Fig. 5.

(1) Pathway 1 of ON evolution is the polymerization of amines with an oxygen-containing molecule. In Fig. 5a, with the decrease of $CHN_{<180Da}$, the intensity of $CHON_{>275Da}$ gradually increases ($r = -0.20$, $p = 0.18$, Fig. S5). They both contain amine groups, and carbon numbers ranges were C6–C12 and C17–C19 for $CHN_{<180Da}$ and $CHON_{>275Da}$, respectively. It is reasonable to hypothesize that $CHON_{>275Da}$ were formed by polymerization of C6–C12 amines with other compounds. Given that C17–C19 amines typically contain alcohol or carboxylic acid groups, the polymerization likely involves additional oxygenated molecules. Previous studies have shown that bimolecular reactions can occur on aqueous surface between amine-carbonyl^{2,86}, amine-carboxylic acid², and amine-Criegee⁸⁷. For example, Duporté et al.⁸⁶ reported that condensed-phase reaction between pinonaldehyde ($C_{10}H_{16}O_2$) and dimethylamine (DMA, C_2H_7N) could generate oligomers including $C_{12}H_{21}ON$, $C_{22}H_{37}O_3N$, and

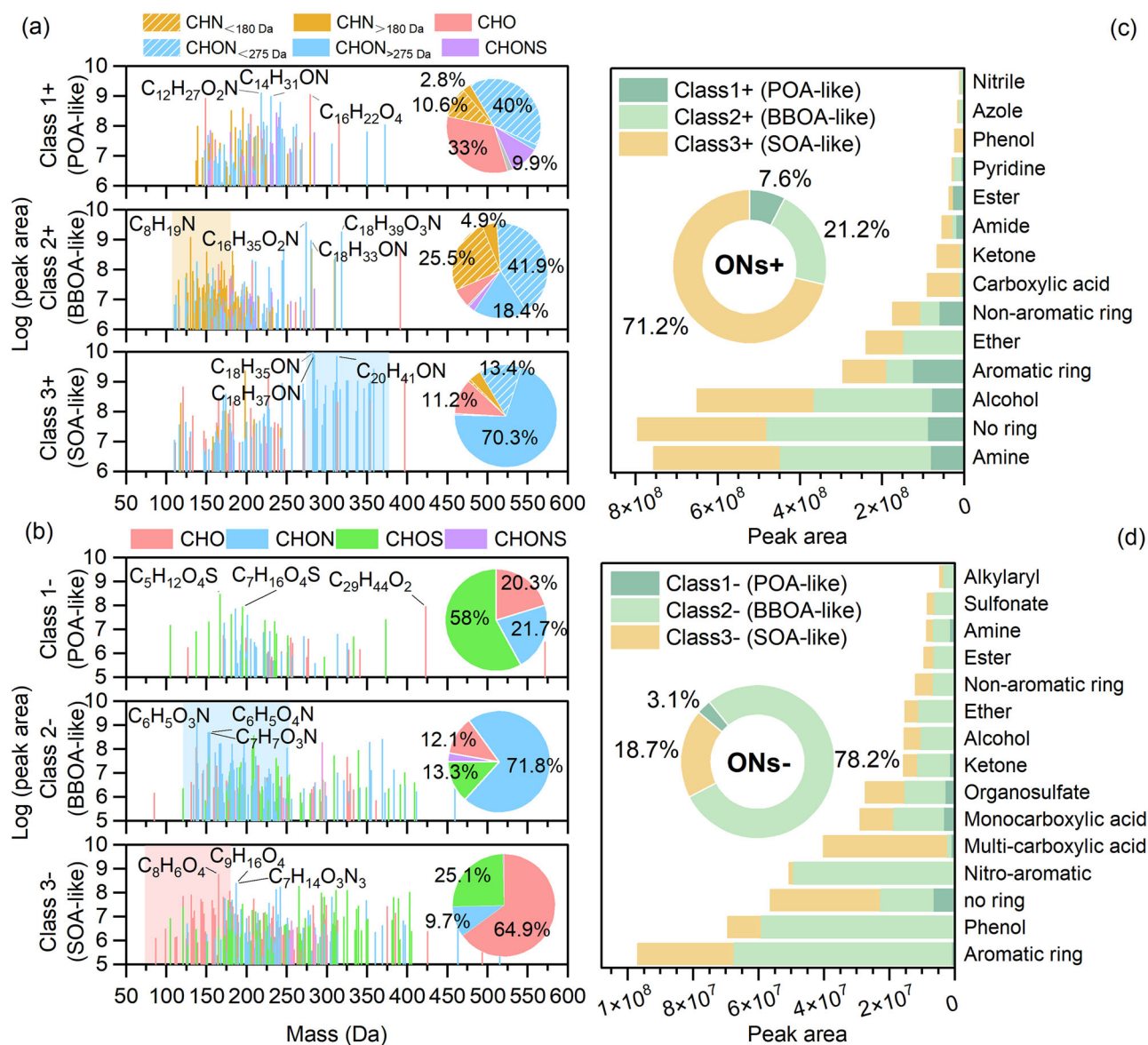


Fig. 4 | Chemical compositional and functional group distribution. **a, b** Mass distribution and species intensity fraction of each class. The chemical formulas of the most abundant substances are labeled in the diagram. $CHN_{<180 Da}$ refers to CHN with molecular weight less than 180 Da, while $CHON_{>275 Da}$ refers to CHON with molecular weight greater than 275 Da. **c, d** Functional group distribution of each

class and fraction of three classes in ONs. ONs + /ONs- represents the nitrogenous organics detected in the positive/negative mode. POA-like, BBOA-like, and SOA-like refer to primary organic aerosol-like, biomass burning organic aerosol-like, and secondary organic aerosol-like, respectively.

$C_{32}H_{53}O_5N$. Furthermore, they pointed out that water could promote dimerization hydrate formation in the heterogeneous reactions, suggesting that the high-humidity conditions observed in our study may be more conducive to heterogeneous amine polymerization reactions.

- (2) Pathway 2 of ON evolution is the ring-opening fragmentation of nitrophenols to form CHO dicarboxylic acids. In Fig. 5b, with the decrease of nitroaromatics, the intensity of CHO dicarboxylic acids increases ($r = -0.20$, $p = 0.19$, Fig. S5). Most CHO dicarboxylic acids are non-ring structures. This suggests that nitroaromatics may undergo ring-opening fragmentation during heterogeneous reactions, yielding lower molecular weight but more oxidized CHO compounds. A study conducted by Wang et al.⁸⁸ revealed that, the aqueous oxidation of primary aromatics at high RH lead to ring-breaking and functionalization to form carbonyls and carboxylic acids. Similarly, Hems et al.³⁷ found that, with aqueous phase photo-oxidation of

nitrophenols, $OH\cdot$ would attack hydroxyl-substitute carbon at an already substituted position, leading to the formation of dicarboxylic acid molecules. For instance, in Hem's study, photo-oxidation fragmentation of nitrocatechol ($C_6H_5O_4N$) would produce maleic acid ($C_4H_4O_4$), a dicarboxylic acid. Similarly, in our study, $C_8H_8O_4$ may be formed by the aqueous phase photo-degradation of $C_8H_5O_4N$. Their functional groups (Table 1) support this hypothesis.

- (3) Pathway 3 of ON evolution is the ring-retaining functionalization of nitroaromatics to form nitroaromatics carboxylic acids. In Fig. 5c, with the decrease of nitroaromatics intensities, the fraction of nitroaromatics containing carboxylic acid groups increase significantly ($r = -0.45$, $p < 0.05$, Fig. S5), indicating the functionalization of nitroaromatics. Previous studies have reported that oxidation of aromatics can generate aromatic carboxylic acids, such as toluene to generate benzoic acid⁸⁹. However, such reactions have not been previously reported for nitroaromatics, deserving further studies. The

Table 1 | Summary of molecular formulas potentially act as markers for biomass burning (Class 2 + and Class 2-) and heterogeneous/aqueous reactions (Class 3+ and Class 3-)

ESI +	Formula	Mass (Da)	RT (min)	Functional group (ring-containing)	Source	ESI-	Formulae	Mass (Da)	RT (min)	Functional group (ring-containing)	Source
1	C ₆ H ₁₄ N ₂	115.12	3.78	Di-amine (Non-aromatic)	BBOA-like	24	C ₆ H ₁₅ O ₅ N	170.01	5.47	Phenol, Nitroaromatic (Aromatic)	BBOA-like
2	C ₇ H ₁₂ N ₂	125.11	4.60	Amine, Nitrile (Non-aromatic)	BBOA-like	25	C ₈ H ₁₆ O ₄ N	178.01	14.56	Phenol, Nitroaromatic (Aromatic)	BBOA-like
3	C ₈ H ₈ N ₂	133.08	2.92	Amine (Aromatic, Non-aromatic)	BBOA-like	26	C ₈ H ₉ O ₄ N	182.05	14.81	Alcohol, Phenol, Nitroaromatic (Aromatic)	BBOA-like
4	C ₈ H ₁₄ N ₂	139.12	6.68	Azole (Aromatic)	BBOA-like	27	C ₆ H ₄ O ₅ N ₂	183.00	13.62	Phenol, Nitroaromatic (Aromatic)	BBOA-like
5	C ₈ H ₁₆ N ₂	141.14	3.25	Di-amine (Non-aromatic)	BBOA-like	28	C ₇ H ₇ O ₅ N	184.03	10.77	Ether, Alkylaryl, Phenol, Nitroaromatic (Aromatic)	BBOA-like
6	C ₉ H ₁₂ N ₂	149.11	5.74	Di-amine (Aromatic)	BBOA-like	29	C ₈ H ₇ O ₅ N	196.03	13.83	Ether, Alkylaryl, Carboxylic acid, Nitroaromatic (Aromatic)	BBOA-like
7	C ₉ H ₁₆ N ₂	153.14	6.84	Di-amine (Non-aromatic)	BBOA-like	30	C ₉ H ₁₁ O ₄ N	196.06	17.08	Ether, Alkylaryl, Phenol, Nitroaromatic (Aromatic)	BBOA-like
8	C ₁₀ H ₁₀ N ₂	159.09	7.86	Pyridine (Aromatic)	BBOA-like	31	C ₇ H ₆ O ₅ N ₂	197.02	17.05	Phenol, Nitroaromatic (Aromatic)	BBOA-like
9	C ₁₀ H ₁₂ N ₂	161.11	9.61	Amine, Pyridine (Aromatic)	BBOA-like	32	C ₇ H ₅ O ₆ N	198.00	11.43	Phenol, Carboxylic acid, Nitroaromatic (Aromatic)	BBOA-like
10	C ₁₀ H ₁₆ N ₂	165.14	9.25	Nitrile (No ring)	BBOA-like	33	C ₈ H ₈ O ₅ N ₂	211.04	18.03	Phenol, Nitroaromatic (Aromatic)	BBOA-like
11	C ₁₀ H ₁₈ N ₂	167.15	9.90	Di-amine (Non-aromatic)	BBOA-like	34	C ₇ H ₆ O ₆ N ₂	213.02	16.15	Phenol, Nitroaromatic (Aromatic)	BBOA-like
12	C ₁₁ H ₈ N ₂	169.08	9.45	Pyridine (Aromatic)	BBOA-like	35	C ₉ H ₁₀ O ₅ N ₂	225.05	19.81	Phenol, Nitroaromatic (Aromatic)	BBOA-like
13	C ₁₀ H ₂₀ N ₂	169.17	9.45	Di-amine (Non-aromatic)	BBOA-like	36	C ₈ H ₈ O ₆ N ₂	227.03	18.12	Phenol, Nitroaromatic (Aromatic)	BBOA-like
14	C ₁₂ H ₁₃ N	172.11	9.86	Amine (Aromatic, Non-aromatic)	BBOA-like	37	C ₆ H ₆ O ₄	143.03	3.82	Di-carboxylic acid (No ring)	SOA-like
15	C ₁₁ H ₁₂ N ₂	173.11	8.96	Azole (Aromatic)	BBOA-like	38	C ₆ H ₁₀ O ₄	145.05	6.37	Di-carboxylic acid (No ring)	SOA-like
16	C ₁₁ H ₁₄ N ₂	175.12	10.14	Amine (Aromatic)	BBOA-like	39	C ₇ H ₁₀ O ₄	157.05	4.31	Di-carboxylic acid (No ring)	SOA-like
17	C ₁₁ H ₁₈ N ₂	179.15	10.91	Di-amine (Non-aromatic)	BBOA-like	40	C ₈ H ₆ O ₄	165.02	7.91	Di-carboxylic acid (Aromatic)	SOA-like
18	C ₁₇ H ₃₇ O ₂ N	288.29	21.04	Alcohol, Amine (No ring)	SOA-like	41	C ₈ H ₁₂ O ₄	171.07	6.33	Di-carboxylic acid (No ring)	SOA-like
19	C ₁₈ H ₃₅ O ₂ N	296.26	24.52	Carboxylic acid, Amine (No ring)	SOA-like	42	C ₇ H ₁₀ O ₅	173.05	2.29	Ketone, Di-carboxylic acid (No ring)	SOA-like
20	C ₁₉ H ₄₁ O ₂ N	316.32	24.06	Alcohol, Amine (No ring)	SOA-like	43	C ₇ H ₁₂ O ₅	175.06	2.66	Alcohol, Di-carboxylic acid (No ring)	SOA-like
ESI-	Formulae	Mass (Da)	RT (min)	Functional group (ring-containing)	Source	44	C ₉ H ₅ O ₄ N	190.01	5.34	Di-carboxylic acid, Nitriles (Aromatic)	SOA-like
21	C ₈ H ₉ O ₄ N	154.01	9.55	Phenol, Nitroaromatic (Aromatic)	BBOA-like	45	C ₁₀ H ₁₉ O ₄ N	216.12	8.98	Di-carboxylic acid, Amine (No ring)	SOA-like
22	C ₈ H ₉ O ₃ N	166.05	17.63	Phenol, Nitroaromatic (Aromatic)	BBOA-like	46	C ₈ H ₅ O ₇ N	226.00	12.85	Phenol, Di-carboxylic acid, Nitroaromatic (Aromatic)	SOA-like
23	C ₇ H ₇ O ₄ N	168.03	13.75	Phenol, Nitroaromatic (Aromatic)	BBOA-like						

"Mass" refers to the mass of the charged ion corresponding to a molecule detected under ESI ± modes in mass spectrometry. "RT" refers to the retention time of compounds detected in liquid chromatography. POA-like, BBOA-like, and SOA-like refer to primary organic aerosol-like, biomass burning organic aerosol-like, and secondary organic aerosol-like, respectively.

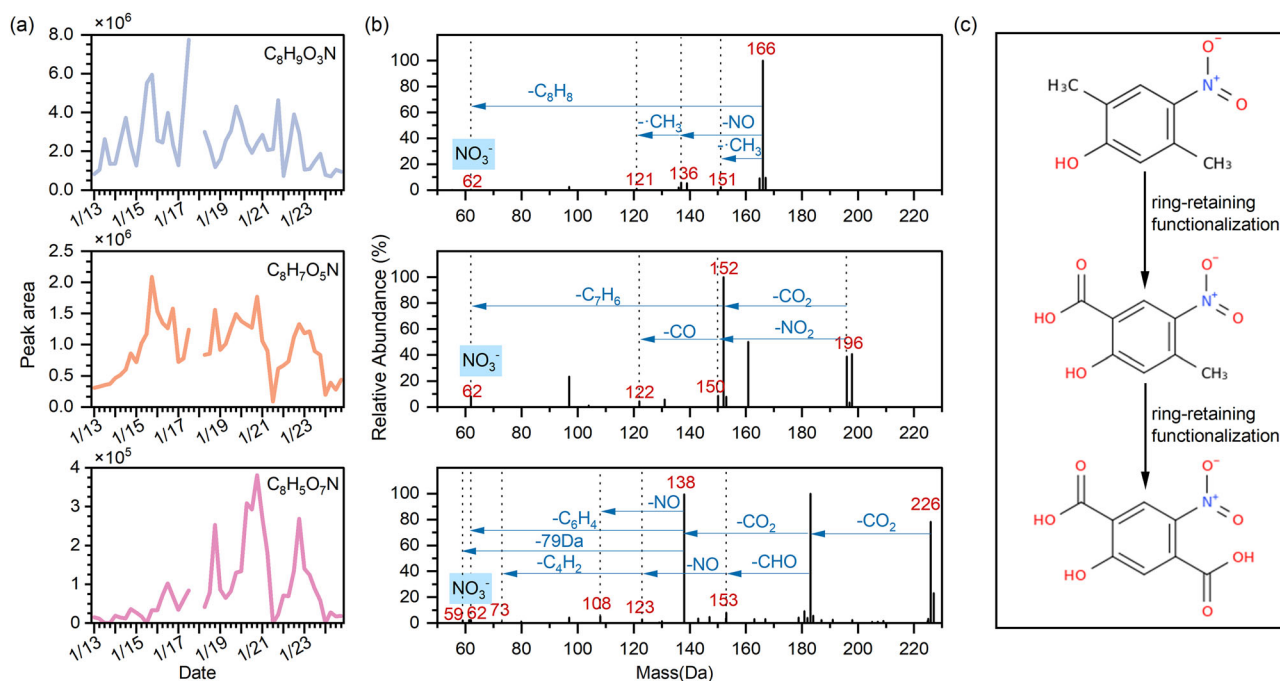


Fig. 6 | Heterogeneous/ aqueous-phase oxidation of a biomass burning-derived nitrophenol. a Timeseries of $C_8H_9O_3N$, $C_8H_7O_5N$, and $C_8H_5O_7N$. **b** The corresponding MS/MS fragmentation patterns of three compounds. **c** Proposed oxidation reaction pathway.

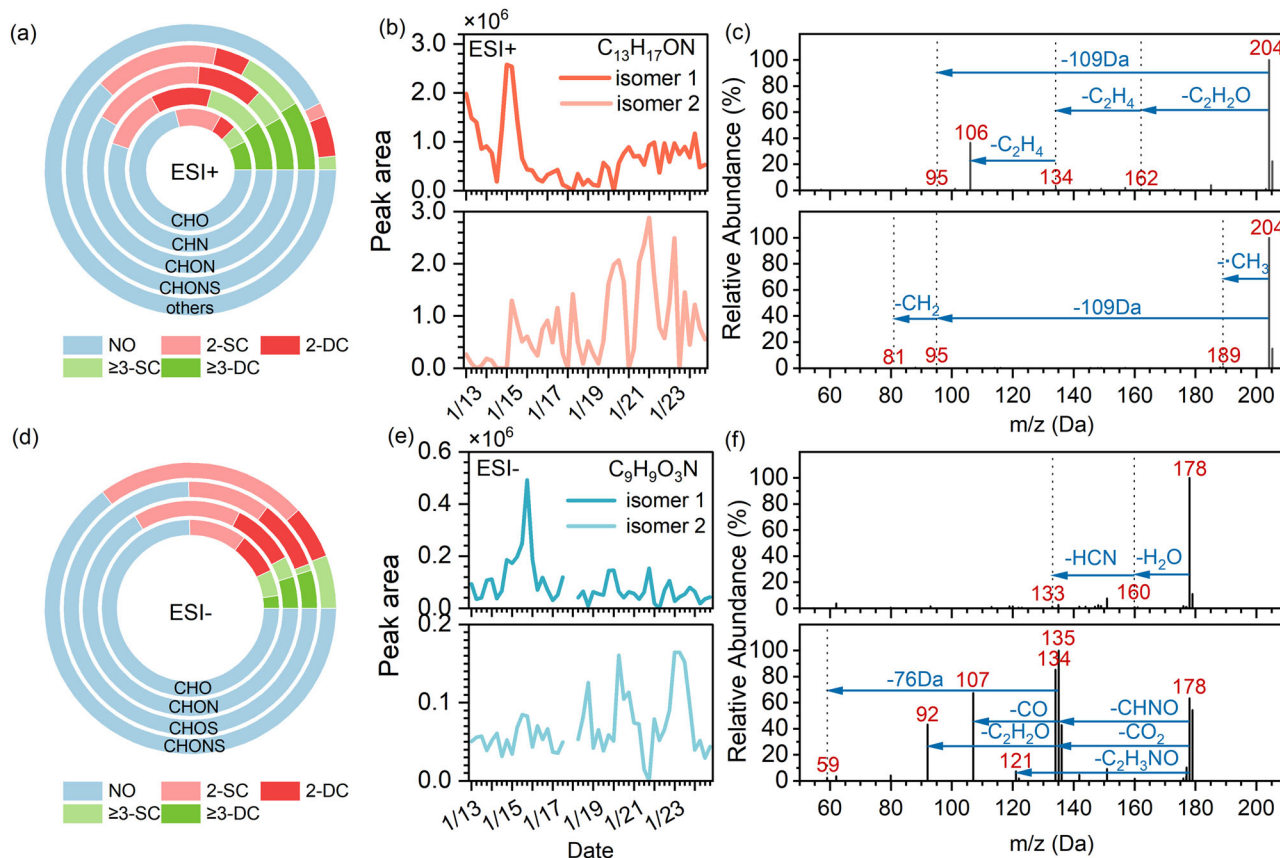


Fig. 7 | Distribution of isomer numbers and sources with representative compounds. a, d The distribution of isomer numbers among various species in ESI+ and ESI-. NO represents no isomers; 2-SC represents two isomers distributed in the same class; 2-DC represents two isomers distributed across different classes, and so on. **b, e** Examples of isomers with significantly different time series. **c, f** MS/MS fragmentation analysis of the corresponding isomers.

(24.3%), which may result from the higher CHONS fraction (16.3%, 17.2%, and 43.4%, in MeOH, ACN, and ACN/water, respectively), while CHON were comparable (12.8%, 6.1%, and 7.0%, respectively). Moreover, the CHOS fraction was significantly higher in ACN/water (31.7%) than in MeOH (12.8%) and acetonitrile (9.5%) (Fig. S1). Overall, methanol extraction yields a broader range of substances but may selectively overestimate nitrogen-containing components while underestimating sulfur-containing constituents.

Quartz filters with a diameter of 50 mm were cut and shredded using methanol-rubbed ceramic scissors. 5 ml of methanol (chromatographically pure) was added to the filters and the extraction was put in an ultrasonic bath for 15 minutes. Ice was added to the ultrasonic bath water to prevent thermal decomposition or volatilization of organic matter. This procedure was repeated three times with same piece of filter and the three extracts were mixed together and then filtered through a 0.22 μm Teflon filter to remove insoluble substances. The filtered sample was purged to almost dryness at 30 °C under a gentle stream of nitrogen and redissolved in 100 μl of methanol. The mean value of the concentration of OC in the sampled PM_{2.5} was 183.87 $\mu\text{g}/\text{m}^3$. The mean value of the solution concentration finally prepared for the MS test by extraction was 1838.73 ng/ μl , with a range of 634.3–3352.67 ng/ μl , and the time series was shown in Fig. S7. The sensitivity of compounds may vary greatly for different species. For example, signal intensity in ESI+ mode is usually several time higher than those in ESI-mode^{20,93}, which also happened in our study. However, the quantification is challenging due to the lack of calibration standards.

2 μl of the extracted solution was analyzed by HPLC (Dionex 3000, Thermo Scientific, USA) coupled to a Q-Exactive Hybrid Quadrupole-Orbitrap mass spectrometer (Thermo scientific, USA). The Thermo Hypersil column (C18, 100 mm \times 2.1 mm, 1.9 μm) was used. The mobile phases were A: 0.1% formic acid in water, B: 0.1% formic acid in acetonitrile, and the gradient elution was performed using a mixture of A and B phases at a flow rate of 300 $\mu\text{l}/\text{min}$. The mass spectrometer was equipped with a heated electrospray ionization source in ESI- and ESI+ modes. All samples were analyzed by MS mode and MS/MS mode in both ESI- and ESI+. The mass resolutions of MS were 140,000 at 200 Da, and the scanning ranges of MS were 50–750 Da. For MS/MS experiment, we employed a Data-Dependent Acquisition (DDA) mode to obtain MS/MS spectra. Precursor ions of intensities $\geq 10,000$ were selected and then fragmented using collision energy of 20 eV, 40 eV. Dynamic exclusion time was set to 10 s.

Before the HPLC analysis, we have optimized the liquid chromatography gradient elution procedures which varied greatly in different references. To determine the best procedures for our samples, we selected four representative chromatographic conditions from previous references for pre-analysis^{19,21,30,94}, and the same actual atmospheric samples in Wuhan was analyzed under the four conditions. The peak times and peak areas of substances with reasonable molecular formulae were compared. As shown in Fig. S8, for all the four conditions, many substances peaked at the same time in the 98% B platform stage, and even more substances peaked after the beginning of the decline. Based on this test, we determined to shorten the gradient rise time and extend the 98% B platform time to improve the separation performance. The improved condition was as follows: the gradient elution conditions were: 5% B for 4 min, increased linearly to 98% B in 31 min and hold for 15 min, back to 5% B in the next 1 min and hold for 9 min. The results after the improvement are shown in Fig. S9, which shows that the peaks of the optimized conditions were better separated at the 98% B platform stage, more substances were detected in the rising stage of the previous gradient, and the peaks of the optimized conditions were reduced after the descending stage. Linearity tests were performed on samples of different concentrations, and most of the compound peak areas and substance concentrations conformed to a linear pattern, so the variation of peak area in different samples can represent the variation in its concentration. Overall, the optimized conditions showed a significant improvement in the separation performance and were used for subsequent sample analysis.

It should be noted that the measured organics in our study cannot represent all the particulate organic compounds, due to the selectivity of

extraction and measuring methods. Firstly, we used methanol to extract organics. Although it is the most-widely used solvent for HPLC detection (Table S2) and are shown to extract more molecules than acetonitrile⁹⁵ and acetonitrile/water, it may still miss a lot of less polar compounds. Secondly, the ability of HPLC to separate compounds is highly dependent on the solvent and the column. The Thermo Hypersil column (C18, 100 mm \times 2.1 mm, 1.9 μm) and the mobile phases of water and acetonitrile that we chose are more suitable for the detection of polar compounds⁹⁶. Thirdly, the ESI source can also only detect compounds with medium to high polarity, and hydrocarbons such as alkanes and olefins cannot be detected⁹⁷.

Data processing of the molecular-level organic composition

Xcalibur (V4.2, Thermo Scientific, USA) software, the non-targeted analysis software MZmine (V3.4.16, Mzio, Germany), and MATLAB (R2023a, The MathWorks, USA) were used for data processing of MS. The HPLC-MS spectra was first processed using Xcalibur to subtract the background. Then the peaks were processed and the molecular formula was fitted by MZmine, and the detailed processing steps and parameter settings of MZmine software were referred to the previous literature^{19,20,30}. The final molecular formula was expressed as C_cH_hO_oN_nS_s, where c, h, o, n, and s correspond to the numbers of C, H, O, N, and S in the molecular formula, respectively. The molecular formulas were batch processed using MATLAB software programming to derive the number of each atom. In order to ensure the accuracy of the peak list and obtain a more rational molecular formula, we selected species that fulfill the following conditions: (1) signal intensity higher than 1000 for ESI+ and higher than 100 for ESI-; (2) signal-to-noise ratios greater than 10; (3) the corresponding chromatographic peaks of the compounds were checked one by one for plausibility and isomerism using the Xcalibur software, and only substances with good peak shapes were selected; (4) the elemental ratios were limited to 0.3–3.0 H/C, 0–3.0 O/C, 0–1.3 N/C, and 0–0.8 S/C. After manual check, about 2200 and 2100 compounds were identified in ESI+ and ESI- modes, respectively.

For the extraction of MS/MS spectra and functional group analysis. Firstly, we used MZmine software to match product ions with corresponding precursor ions to extract MS/MS spectra, and then imported it into SIRIUS (V6.0.7, San Diego Supercomputer Center, USA) for molecular structure identification. SIRIUS merging CSI: FingerID search services has excellent identification accuracy at small-molecule identification⁹⁸ and has been used in atmospherically relevant studies^{21,30,40}. In SIRIUS, we limited ionization adducts to [M + H]⁺ and [M – H][–], mass tolerance to 3 ppm. The top scoring candidate structure's SMILES (Simplified Molecular Input Line Entry System) which can explicitly describe molecular structures using ASCII strings were exported from SIRIUS for further analysis. Finally, we applied APRL Substructure Search Program⁹⁹ to enumerate atmospherically relevant functional groups, and if the number of compounds containing a certain functional group is less than 10, we will not further analyze that functional group.

Statistical analysis

Through MATLAB batch processing, each organic compound was given a time series showing its peak area variation during the 12 days. We found that the time series for different organics showed different trends. Therefore, we clustered the time series using K-Means clustering algorithm¹⁰⁰. K-Means clustering algorithm is a common clustering method that classifies the time series to several classes. Time series of substances with more than or equal to 30 data points were selected for clustering to ensure reliability.

The sulfur oxidation ratio (SOR) and the nitrogen oxidation rate (NOR) calculated by Eq. S1 and Eq. S2 can represent the oxidation fraction of primary SO₂ and NO_x to secondary particulate sulfate and nitrate, respectively. Aerosol liquid water (ALW), were modeled by ISORROPIA II^{79,101,102} and calculated by Eq. S3 and Eq. S4, to indicate the extent of aqueous/heterogeneous reactions. The concentration of SO₄^{2–}, NO₃[–], Cl[–], NH₄⁺, particulate metals, ambient temperature, and relative humidity were

input to the ISORROPIA II model. The reverse mode and metastable mode were selected as previously described⁷⁹.

MeteoInfo software was used for the backward trajectory analysis and air mass clustering. The input meteorological data during Jan. 2018 was obtained from the National Oceanic and Atmospheric Administration (NOAA). To facilitate specific analysis of air mass trajectories during heavy pollution periods and to trace pollution sources, a -72h backward trajectory was generated every hour. Since the main range of human activity is within 200 m of the surface, the starting height of the air masses was set to 200 meters. Fire spot data was downloaded from NASA FIRMS Web Fire Mapper and could be accessible at <https://firms.modaps.eosdis.nasa.gov/>¹⁰³ (last accessed: 13 June 2025).

Data availability

Data and code are available upon request from the corresponding authors.

Received: 15 January 2025; Accepted: 5 June 2025;

Published online: 01 July 2025

References

1. Yu, X. et al. New measurements reveal a large contribution of nitrogenous molecules to ambient organic aerosol. *npj Clim. Atmos. Sci.* **7**, 72 (2024).
2. Qiu, C. & Zhang, R. Multiphase chemistry of atmospheric amines. *Phys. Chem. Chem. Phys.* **15**, 5738 (2013).
3. Laskin, A., Laskin, J. & Nizkorodov, S. A. Chemistry of atmospheric brown carbon. *Chem. Rev.* **115**, 4335–4382 (2015).
4. Duce, R. A. et al. Impacts of atmospheric anthropogenic nitrogen on the open ocean. *Science* **320**, 893–897 (2008).
5. Kitanovski, Z., Grgic, I., Vermeylen, R., Claeys, M. & Maenhaut, W. Liquid chromatography tandem mass spectrometry method for characterization of monoaromatic nitro-compounds in atmospheric particulate matter. *Journal of Chromatography A* **1268**, 35–43 (2012).
6. Iinuma, Y., Böge, O., Gräfe, R. & Herrmann, H. Methyl-nitrocatechols: atmospheric tracer compounds for biomass burning secondary organic aerosols. *Environ. Sci. Technol.* **44**, 8453–8459 (2010).
7. Yu, X., Wong, Y. K. & Yu, J. Z. Abundance and sources of organic nitrogen in fine (PM_{2.5}) and coarse (PM_{2.5–10}) particulate matter in urban Hong Kong. *Sci. Total Environ.* **901**, 165880 (2023).
8. Rastogi, N., Zhang, X., Edgerton, E. S., Ingall, E. & Weber, R. J. Filterable water-soluble organic nitrogen in fine particles over the southeastern USA during summer. *Atmos. Environ.* **45**, 6040–6047 (2011).
9. Zhang, Q. et al. Organic nitrogen in PM_{2.5} in Beijing. *Front. Environ. Sci. Eng.* **9**, 1004–1014 (2015).
10. Hallquist, M. et al. The formation, properties and impact of secondary organic aerosol: current and emerging issues. *Atmospheric Chemistry and Physics* **9**, 5155–5236 (2009).
11. Kiendler-Scharr, A. et al. Ubiquity of organic nitrates from nighttime chemistry in the European submicron aerosol. *Geophys. Res. Lett.* **43**, 7735–7744 (2016).
12. Lin, P., Yu, J. Z., Engling, G. & Kalberer, M. Organosulfates in humic-like substance fraction isolated from aerosols at seven locations in East Asia: A study by ultra-high-resolution mass spectrometry. *Environ. Sci. Technol.* **46**, 13118–13127 (2012).
13. Song, J. et al. Molecular characterization of water-soluble humic like substances in smoke particles emitted from combustion of biomass materials and coal using ultrahigh-resolution electrospray ionization fourier transform ion cyclotron resonance mass spectrometry. *Environ. Sci. Technol.* **52**, 2575–2585 (2018).
14. Altieri, K. E., Turpin, B. J. & Seitzinger, S. P. Oligomers, organosulfates, and nitrooxy organosulfates in rainwater identified by ultra-high resolution electrospray ionization FT-ICR mass spectrometry. *Atmos. Chem. Phys.* **9**, 2533–2542 (2009).
15. Le Breton, M. et al. Online gas- and particle-phase measurements of organosulfates, organosulfonates and nitrooxy organosulfates in Beijing utilizing a FIGAERO ToF-CIMS. *Atmos. Chem. Phys.* **18**, 10355–10371 (2018).
16. Surratt, J. D. et al. Organosulfate formation in biogenic secondary organic aerosol. *J. Phys. Chem. A* **112**, 8345–8378 (2008).
17. Surratt, J. D. et al. Evidence for organosulfates in secondary organic aerosol. *Environ. Sci. Technol.* **41**, 517–527 (2007).
18. Wang, K., Zhang, Y., Huang, R.-J., Cao, J. & Hoffmann, T. UHPLC-Orbitrap mass spectrometric characterization of organic aerosol from a central European city (Mainz, Germany) and a Chinese megacity (Beijing). *Atmos. Environ.* **189**, 22–29 (2018).
19. Wang, X. et al. Chemical characteristics of organic aerosols in Shanghai: A study by ultrahigh-performance liquid chromatography coupled with orbitrap mass spectrometry. *J. Geophys. Res. Atmos.* **122**, 11,703–11,722 (2017).
20. Wang, W. et al. Molecular characterization of organic aerosols in Taiyuan, China: Seasonal variation and source identification. *Sci. Total Environ.* **800**, 149419 (2021).
21. Wang, Z., Ge, Y., Bi, S., Liang, Y. & Shi, Q. Molecular characterization of organic aerosol in winter from Beijing using UHPLC-Orbitrap MS. *Sci. Total Environ.* **812**, 151507 (2022).
22. Zuth, C., Vogel, A. L., Ockenfeld, S., Huesmann, R. & Hoffmann, T. Ultrahigh-resolution mass spectrometry in real time: atmospheric pressure chemical ionization orbitrap mass spectrometry of atmospheric organic aerosol. *Anal. Chem.* **90**, 8816–8823 (2018).
23. Jiang, B. et al. Molecular composition of urban organic aerosols on clear and hazy days in Beijing: a comparative study using FT-ICR MS. *Environ. Chem.* **13**, 888 (2016).
24. Nozière, B. et al. The molecular identification of organic compounds in the atmosphere: State of the art and challenges. *Chem. Rev.* **115**, 3919–3983 (2015).
25. Dron, J. et al. Functional group composition of ambient and source organic aerosols determined by tandem mass spectrometry. *Atmos. Chem. Phys.* **10**, 7041–7055 (2010).
26. Huang, R.-J. et al. Chromophoric fingerprinting of brown carbon from residential biomass burning. *Environ. Sci. Technol. Lett.* **9**, 102–111 (2022).
27. Wang, Z., Chen, X., Liang, Y. & Shi, Q. Molecular characterization of carbonyl compounds in atmospheric fine particulate matters (PM_{2.5}) in Beijing by derivatization with Girard's reagent T combined with positive-ion ESI Orbitrap MS. *Atmos. Res.* **273**, 106176 (2022).
28. Da Silva, R. R. et al. Propagating annotations of molecular networks using in silico fragmentation. *PLoS Comput Biol.* **14**, e1006089 (2018).
29. Schymanski, E. L. et al. Critical assessment of small molecule identification 2016: automated methods. *J. Cheminform* **9**, 22 (2017).
30. Wan, Y. et al. Nontarget tandem high-resolution mass spectrometry analysis of functionalized organic compounds in atmospherically relevant samples. *Environ. Sci. Technol. Lett.* **9**, 1022–1029 (2022).
31. Dron, J., Abidi, E., Haddad, I. E., Marchand, N. & Wortham, H. Precursor ion scanning-mass spectrometry for the determination of nitro functional groups in atmospheric particulate organic matter. *Anal. Chim. Acta* **618**, 184–195 (2008).
32. Cai, B. et al. Rapid aqueous-phase dark reaction of phenols with nitrosonium ions: Novel mechanism for atmospheric nitrosation and nitration at low pH. *PNAS Nexus* **3**, pgae385 (2024).
33. Hems, R. F., Schnitzler, E. G., Liu-Kang, C., Cappa, C. D. & Abbatt, J. P. D. Aging of atmospheric brown carbon aerosol. *ACS Earth Space Chem.* **5**, 722–748 (2021).
34. Slade, J. H. & Knopf, D. A. Multiphase OH oxidation kinetics of organic aerosol: The role of particle phase state and relative humidity. *Geophys. Res. Lett.* **41**, 5297–5306 (2014).

35. Witkowski, B., Jain, P. & Gierczak, T. Aqueous chemical bleaching of 4-nitrophenol brown carbon by hydroxyl radicals; products, mechanism, and light absorption. *Atmos. Chem. Phys.* **22**, 5651–5663 (2022).
36. Bejan, I. G., Olariu, R.-I. & Wiesen, P. Secondary organic aerosol formation from nitrophenols photolysis under atmospheric conditions. *Atmosphere* **11**, 1346 (2020).
37. Hems, R. F. & Abbatt, J. P. D. Aqueous phase photo-oxidation of brown carbon nitrophenols: Reaction kinetics, mechanism, and evolution of light absorption. *ACS Earth Space Chem.* **2**, 225–234 (2018).
38. Takeuchi, M. & Ng, N. L. Organic Nitrates and Secondary Organic Aerosol (SOA) Formation from Oxidation of Biogenic Volatile Organic Compounds. in *ACS Symposium Series* (eds. Hunt, S. W., Laskin, A. & Nizkorodov, S. A.) **1299** 105–125 (American Chemical Society, Washington, DC, 2018).
39. Liebmann, J. et al. Alkyl nitrates in the boreal forest: formation via the NO₃⁻, OH⁻ and O₃-induced oxidation of biogenic volatile organic compounds and ambient lifetimes. *Atmos. Chem. Phys.* **19**, 10391–10403 (2019).
40. Ditto, J. C. et al. Nontargeted tandem mass spectrometry analysis reveals diversity and variability in aerosol functional groups across multiple sites, seasons, and times of day. *Environ. Sci. Technol. Lett.* **7**, 60–69 (2020).
41. Boyd, C. M. et al. Secondary organic aerosol formation from the β-pinene+NO₃ system: Effect of humidity and peroxy radical fate. *Atmos. Chem. Phys.* **15**, 7497–7522 (2015).
42. Bates, K. H., Burke, G. J. P., Cope, J. D. & Nguyen, T. B. Secondary organic aerosol and organic nitrogen yields from the nitrate radical (NO₃) oxidation of alpha-pinene from various RO₂ fates. *Atmos. Chem. Phys.* **22**, 1467–1482 (2022).
43. Zhai, S. et al. Fine particulate matter (PM_{2.5}) trends in China, 2013–2018: separating contributions from anthropogenic emissions and meteorology. *Atmos. Chem. Phys.* **19**, 11031–11041 (2019).
44. Shen, L. et al. Changes in the distribution pattern of PM_{2.5} pollution over central China. *Remote Sens.* **13**, 4855 (2021).
45. Jin, S., Ma, Y., Gong, W. & Zhang, M. Temporal-spatial changes in aerosols during winter haze of wuhan: a typical high-humid inland city in central china. *Int. Arch. Photogramm. Remote Sens. Spat. Inf. Sci.* **XLIII-B3-2020**, 807–812 (2020).
46. Lu, M. et al. Investigating the Transport Mechanism of PM_{2.5} Pollution during January 2014 in Wuhan, Central China. *Adv. Atmos. Sci.* **36**, 1217–1234 (2019).
47. Hui, L. et al. VOC characteristics, sources and contributions to SOA formation during haze events in Wuhan, Central China. *Sci. Total Environ.* **650**, 2624–2639 (2019).
48. Wang, S. et al. Characteristics and origins of air pollutants in Wuhan, China, based on observations and hybrid receptor models. *Journal of the Air & Waste Management Association* **67**, 739–753 (2017).
49. Yu, C. et al. Heavy air pollution with a unique “non-stagnant” atmospheric boundary layer in the Yangtze River middle basin aggravated by regional transport of PM_{2.5} over China. *Atmos. Chem. Phys.* **20**, 7217–7230 (2020).
50. Wu, J. et al. Estimating the open biomass burning emissions in central and eastern China from 2003 to 2015 based on satellite observation. *Atmos. Chem. Phys.* **18**, 11623–11646 (2018).
51. Zhang, L., Liu, Y. & Hao, L. Contributions of open crop straw burning emissions to PM_{2.5} concentrations in China. *Environ. Res. Lett.* **11**, 014014 (2016).
52. Li, R. et al. Estimating emissions from crop residue open burning in central China from 2012 to 2020 using statistical models combined with satellite observations. *Remote Sens.* **14**, 3682 (2022).
53. Mehmood, K. et al. Spatial and temporal distributions of air pollutant emissions from open crop straw and biomass burnings in China from 2002 to 2016. *Environ. Chem. Lett.* **16**, 301–309 (2018).
54. Peng, K., Jiang, W. & Deng, Y. Identification of wetland damage degree and analysis of its driving forces in Wuhan Urban Agglomeration (in Chinese). *J. Nat. Resour.* **34**, 1694–1707 (2019).
55. Mao, J. et al. Molecular characterization of nitrogen-containing organic compounds in the winter North China Plain. *Sci. Total Environ.* **838**, 156189 (2022).
56. Wang, K. et al. Urban organic aerosol composition in eastern China differs from north to south: molecular insight from a liquid chromatography–mass spectrometry (Orbitrap) study. *Atmos. Chem. Phys.* **21**, 9089–9104 (2021).
57. Xu, L., Suresh, S., Guo, H., Weber, R. J. & Ng, N. L. Aerosol characterization over the southeastern united states using high-resolution aerosol mass spectrometry: Spatial and seasonal variation of aerosol composition and sources with a focus on organic nitrates. *Atmos. Chem. Phys.* **15**, 7307–7336 (2015).
58. Leaitch, W. R. et al. Organic functional groups in the submicron aerosol at 82.5° N, 62.5° W from 2012 to 2014. *Atmos. Chem. Phys.* **18**, 3269–3287 (2018).
59. Russell, L. M., Bahadur, R. & Ziemann, P. J. Identifying organic aerosol sources by comparing functional group composition in chamber and atmospheric particles. *Proc. Natl Acad. Sci.* **108**, 3516–3521 (2011).
60. Ng, N. L. et al. Nitrate radicals and biogenic volatile organic compounds: Oxidation, mechanisms, and organic aerosol. *Atmos. Chem. Phys.* **17**, 2103–2162 (2017).
61. Rindelaub, J. D. et al. The acid-catalyzed hydrolysis of an α-pinene-derived organic nitrate: Kinetics, products, reaction mechanisms, and atmospheric impact. *Atmos. Chem. Phys.* **16**, 15425–15432 (2016).
62. Xu, L. et al. Source identification of PM_{2.5} at a port and an adjacent urban site in a coastal city of China: Impact of ship emissions and port activities. *Sci. Total Environ.* **634**, 1205–1213 (2018).
63. Liu, B. et al. Source apportionment of atmospheric pollutants based on the online data by using PMF and ME2 models at a megacity, China. *Atmos. Res.* **185**, 22–31 (2017).
64. Moreira, T. C. L. et al. Intra-urban biomonitoring: Source apportionment using tree barks to identify air pollution sources. *Environ. Int.* **91**, 271–275 (2016).
65. Paulauskas, R. et al. Online determination of potassium and sodium release behaviour during single particle biomass combustion by FES and ICP-MS. *Sci. Total Environ.* **746**, 141162 (2020).
66. Shi, J. et al. Characteristics of PM_{2.5} Components in the Urban Atmosphere of Lincang City and the Influence of Transboundary Biomass Burning (in Chinese). *Environ. Chem.* **43**, 1–13 (2024).
67. Chantara, S., Thepnuan, D., Wiriya, W., Prawan, S. & Tsai, Y. I. Emissions of pollutant gases, fine particulate matters and their significant tracers from biomass burning in an open-system combustion chamber. *Chemosphere* **224**, 407–416 (2019).
68. Waked, A. et al. Source apportionment of PM₁₀ in a north-western Europe regional urban background site (Lens, France) using positive matrix factorization and including primary biogenic emissions. *Atmos. Chem. Phys.* **14**, 3325–3346 (2014).
69. Amato, F. et al. Size and time-resolved roadside enrichment of atmospheric particulate pollutants. *Atmos. Chem. Phys.* **11**, 2917–2931 (2011).
70. Liu, T. et al. Characteristics, Origins, and Atmospheric Processes of Amines in Fine Aerosol Particles in Winter in China. *JGR Atmos.* **128**, e2023JD038974 (2023).
71. Corral, A. F. et al. Dimethylamine in cloud water: A case study over the northwest Atlantic Ocean. *Environ. Sci.: Atmos.* **2**, 1534–1550 (2022).
72. You, Y. et al. Atmospheric amines and ammonia measured with a chemical ionization mass spectrometer (CIMS). *Atmos. Chem. Phys.* **14**, 12181–12194 (2014).
73. Wang, L. et al. Observations of fine particulate nitrated phenols in four sites in northern China: Concentrations, source apportionment, and secondary formation. *Atmos. Chem. Phys.* **18**, 4349–4359 (2018).

74. Salvador, C. M. G. et al. Ambient nitro-aromatic compounds – biomass burning versus secondary formation in rural China. *Atmos. Chem. Phys.* **21**, 1389–1406 (2021).
75. Kitanovski, Z., Grgić, I., Yasmeen, F., Claeys, M. & Čusak, A. Development of a liquid chromatographic method based on ultraviolet–visible and electrospray ionization mass spectrometric detection for the identification of nitrocatechols and related tracers in biomass burning atmospheric organic aerosol. *Rapid Comm. Mass Spectrom.* **26**, 793–804 (2012).
76. Mohr, C. et al. Contribution of nitrated phenols to wood burning brown carbon light absorption in detling, United Kingdom during Winter Time. *Environ. Sci. Technol.* **47**, 6316–6324 (2013).
77. Kahnt, A. et al. One-year study of nitro-organic compounds and their relation to wood burning in PM10 aerosol from a rural site in Belgium. *Atmos. Environ.* **81**, 561–568 (2013).
78. Leung, C. W., Wang, X. & Hu, D. Characteristics and source apportionment of water-soluble organic nitrogen (WSON) in PM2.5 in Hong Kong: With focus on amines, urea, and nitroaromatic compounds. *J. Hazard. Mater.* **469**, 133899 (2024).
79. Li, X. et al. Interactions between aerosol organic components and liquid water content during haze episodes in Beijing. *Atmos. Chem. Phys.* **19**, 12163–12174 (2019).
80. Xu, W. et al. Effects of Aqueous-Phase and Photochemical Processing on Secondary Organic Aerosol Formation and Evolution in Beijing, China. *Environ. Sci. Technol.* **51**, 762–770 (2017).
81. Chen, T. et al. Effect of relative humidity on SOA formation from aromatic hydrocarbons: Implications from the evolution of gas- and particle-phase species. *Sci. Total Environ.* **773**, 145015 (2021).
82. Deetz, K. et al. Aerosol liquid water content in the moist southern west african monsoon layer and its radiative impact. *Atmos. Chem. Phys.* **18**, 14271–14295 (2018).
83. Haslett, S. L. et al. The radiative impact of out-of-cloud aerosol hygroscopic growth during the summer monsoon in southern west Africa. *Atmos. Chem. Phys.* **19**, 1505–1520 (2019).
84. Liu, P. et al. Formation mechanisms of atmospheric nitrate and sulfate during the winter haze pollution periods in Beijing: gas-phase, heterogeneous and aqueous-phase chemistry. *Atmos. Chem. Phys.* **20**, 4153–4165 (2020).
85. Li, G. et al. A possible pathway for rapid growth of sulfate during haze days in China. *Atmos. Chem. Phys.* **17**, 3301–3316 (2017).
86. Duporté, G. et al. Nitrogen-Containing Low Volatile Compounds from Pinonaldehyde-Dimethylamine Reaction in the Atmosphere: A Laboratory and Field Study. *Environ. Sci. Technol.* **50**, 4693–4700 (2016).
87. Kumar, M. & Francisco, J. S. Elucidating the molecular mechanisms of Criegee-amine chemistry in the gas phase and aqueous surface environments. *Chem. Sci.* **10**, 743–751 (2019).
88. Wang, J. et al. Aqueous production of secondary organic aerosol from fossil-fuel emissions in winter Beijing haze. *Proc. Natl Acad. Sci.* **118**, e2022179118 (2021).
89. Hamilton, J., Webb, P., Lewis, A. & Reviejo, M. Quantifying small molecules in secondary organic aerosol formed during the photo-oxidation of toluene with hydroxyl radicals. *Atmos. Environ.* **39**, 7263–7275 (2005).
90. He, Q. et al. Optical properties of secondary organic aerosol produced by photooxidation of naphthalene under NOx condition. *Environ. Sci. Technol.* **56**, 4816–4827 (2022).
91. Shakya, K. M. & Griffin, R. J. Secondary organic aerosol from photooxidation of polycyclic aromatic hydrocarbons. *Environ. Sci. Technol.* **44**, 8134–8139 (2010).
92. Wang, Z. et al. Variations in the oxidation potential of PM2.5 in an old industrial city in China from 2015 to 2018. *Sci. Total Environ.* **948**, 174639 (2024).
93. Wang, W. et al. Influence of COVID-19 lockdown on the variation of organic aerosols: Insight into its molecular composition and oxidative potential. *Environ. Res.* **206**, 112597 (2022).
94. López, A., Fuentes, E., Yusà, V., Ibáñez, M. & Coscollà, C. Identification of unknown substances in ambient air (PM10), profiles and differences between Rural, Urban and Industrial Areas. *Toxics* **10**, 220 (2022).
95. Li, H. et al. Molecular characterization of organosulfur and organonitrogen compounds in summer and winter PM2.5 via UHPLC-Q-orbitrap MS/MS. *Environ. Sci. Technol.* **58**, 21692–21701 (2024).
96. Rudakov, O. B., Rudakova, L. V. & Selemenev, V. F. Acetonitrile as tops solvent for liquid chromatography and extraction. *JACS* **6**, 883 (2023).
97. Wilm, M. Principles of electrospray ionization. *Mol. Cell. Proteom.* **10**, M111.009407 (2011).
98. Dührkop, K. et al. SIRIUS 4: A rapid tool for turning tandem mass spectra into metabolite structure information. *Nat. Methods* **16**, 299–302 (2019).
99. Ruggeri, G. & Takahama, S. Technical note: Development of chemoinformatic tools to enumerate functional groups in molecules for organic aerosol characterization. *Atmos. Chem. Phys.* **16**, 4401–4422 (2016).
100. Peng, Y. A Presentation of Time Series Algorithm Based on K-Mean and Its Application in Clustering. in *2019 2nd International Conference on Intelligent Systems Research and Mechatronics Engineering (ISRME 2019)* 358–361 (Francis Press, Taiyuan, 2019).
101. Continued development and testing of a new thermodynamic aerosol module for urban and regional air quality models. *Atmos. Environ.* **33**, 1553–1560 (1999).
102. Nenes, A., Pandis, S. N. & Pilinis, C. ISORROPIA: A new thermodynamic equilibrium model for multiphase multicomponent inorganic aerosols. *Aquat. Geochem.* **4**, 123–152 (1998).
103. Ren, B. et al. Use of the PSCF method to analyze the variations of potential sources and transports of NO2, SO2, and HCHO observed by MAX-DOAS in Nanjing, China during 2019. *Sci. Total Environ.* **782**, 146865 (2021).

Acknowledgements

This study was supported by the National Natural Science Foundation of China (22376166 and 42277093), the Fundamental Research Funds for the Central Universities (2042024kf0013), and Natural Science Foundation of Hubei Province (2023AFB768 and 2023AFA057).

Author contributions

X.L., H.C., X.H., and P.Z. designed the study. X.H. and P.Z. participated in data collection and analysis, prepared the manuscript with contributions from all co-authors. All authors approved the final version of the manuscript.

Competing interests

The authors declare no competing interests.

Additional information

Supplementary information The online version contains supplementary material available at <https://doi.org/10.1038/s41612-025-01118-5>.

Correspondence and requests for materials should be addressed to Xiaoxiao Li or Hairong Cheng.

Reprints and permissions information is available at <http://www.nature.com/reprints>

Publisher's note Springer Nature remains neutral with regard to jurisdictional claims in published maps and institutional affiliations.

Open Access This article is licensed under a Creative Commons Attribution 4.0 International License, which permits use, sharing, adaptation, distribution and reproduction in any medium or format, as long as you give appropriate credit to the original author(s) and the source, provide a link to the Creative Commons licence, and indicate if changes were made. The images or other third party material in this article are included in the article's Creative Commons licence, unless indicated otherwise in a credit line to the material. If material is not included in the article's Creative Commons licence and your intended use is not permitted by statutory regulation or exceeds the permitted use, you will need to obtain permission directly from the copyright holder. To view a copy of this licence, visit <http://creativecommons.org/licenses/by/4.0/>.

© The Author(s) 2025

Xuehui He^{1,2,7}, Ping Zeng^{1,7}, Yanping Zhu¹, Shan Xu¹, Haoqian Wang¹, Yibei Wan³, Chunyu Xu¹, Zongyao Lu¹, Xiaomeng Guo¹, Ziwei La¹, Lele Sa¹, Rujing Yin⁴, Zhaojin An^{2,5}, Yanqun Liu⁶, Huan Yu³, Jingkun Jiang², Xiaoxiao Li¹✉ & Hairong Cheng¹✉

¹School of Resources and Environmental Sciences, Wuhan University, Wuhan, China. ²State Key Joint Laboratory of Environment Simulation and Pollution Control, School of Environment, Tsinghua University, Beijing, China. ³Department of Atmospheric Science, School of Environmental Studies, China University of Geosciences, Wuhan, China. ⁴Key Laboratory of Industrial Ecology and Environmental Engineering (Ministry of Education), School of Environmental Science and Technology, Dalian University of Technology, Dalian, China. ⁵School of Engineering and Applied Sciences, Harvard University, Cambridge, MA, USA. ⁶Center for Women's and Children's Health Research, Wuhan University School of Nursing, Research Center for Lifespan Health, Wuhan University, Wuhan, China. ⁷These authors contributed equally: Xuehui He, Ping Zeng. lixiaoxiao@whu.edu.cn; chenghr@whu.edu.cn